photonics

MDPI

Article

Untrained Physics-Informed Deep Learning for Rapid Multifrequency Optical Property Inversion in SFDI

Xudong Wu [1,2], Shuang Yu [1,2,*] and Enzhi Feng [1,2]

[1] Heilongjiang Province Key Laboratory of Laser Spectroscopy Technology and Application, Harbin University of Science and Technology, Harbin 150080, China; 2420610169@stu.hrbust.edu.cn (X.W.); 2510603090@stu.hrbust.edu.cn (E.F.)
[2] School of Measurement–Control Technology and Communications Engineering, Harbin University of Science and Technology, Harbin 150080, China
* Correspondence: yushuang@hrbust.edu.cn

Abstract

Spatial frequency domain imaging (SFDI) is a wide-field, non-contact optical technique that enables quantitative mapping of tissue optical properties. Multi-frequency SFDI reduces inversion ambiguity, but conventional least-squares fitting is computationally expensive, limiting clinical translation. Here, we present an untrained physics-informed deep learning framework for image-domain inversion of absorption (μ_a) and reduced scattering (μ'_s) coefficients from multi-frequency diffuse reflectance. A diffusion-approximation forward model is embedded as a loss term, which eliminates the need for ground-truth training datasets and mitigates overfitting. The network takes multi-frequency diffuse reflectance matrices and corresponding spatial-frequency matrices as input and outputs paired μ_a and μ'_s maps. Compared with least-squares fitting, the proposed method reduced multi-frequency optical property inversion time from over twenty minutes to under two minutes, corresponding to an approximately 11-fold speedup. Its performance was demonstrated in simulations and phantom validation, and its feasibility was further shown in in vivo measurements. This untrained physics-informed deep learning approach enables rapid multi-frequency optical property inversion in wide-field SFDI and holds great promise for its translation to real-world applications.

Keywords: spatial frequency domain imaging; multi-frequency; optical property inversion; untrained deep learning

1. Introduction

Spatial frequency domain imaging (SFDI) is a non-invasive, wide-field optical imaging modality that provides quantitative maps of tissue optical properties, including the absorption coefficient μ_a and the reduced scattering coefficient μ'_s. These parameters encode important physical and chemical information about tissue composition and microstructure and have broad potential in biomedical applications such as disease detection, tissue characterization, and image-guided therapy [1,2]. SFDI has been widely applied in biomedical and agricultural fields, including hemoglobin concentration measurement, postoperative monitoring, dermatology and aesthetic medicine, and fruit quality assessment [3–7]. The instrumentation and technical details of SFDI have been described elsewhere [8–14]. Briefly, spatially modulated illumination patterns are projected onto the sample surface, and the reflected light is captured by a camera (Figure 1). The acquired images are demodulated and calibrated to obtain the diffuse reflectance at each pixel for each spatial frequency [12–14].

Check for updates

Received: 20 October 2026
Revised: 15 November 2026
Accepted: 23 November 2026
Published: 26 November 2026

Copyright: © 2026 by the authors. Licensee MDPI, Basel, Switzerland. This article is an open access article distributed under the terms and conditions of the Creative Commons Attribution (CC BY) license.

The resulting diffuse reflectance R_d and corresponding spatial frequency f_x are then used as inputs to an inversion model, which retrieves μ_a and μ'_s pixel-wise. Figure 2 illustrates the data flow for SFDI optical property extraction.

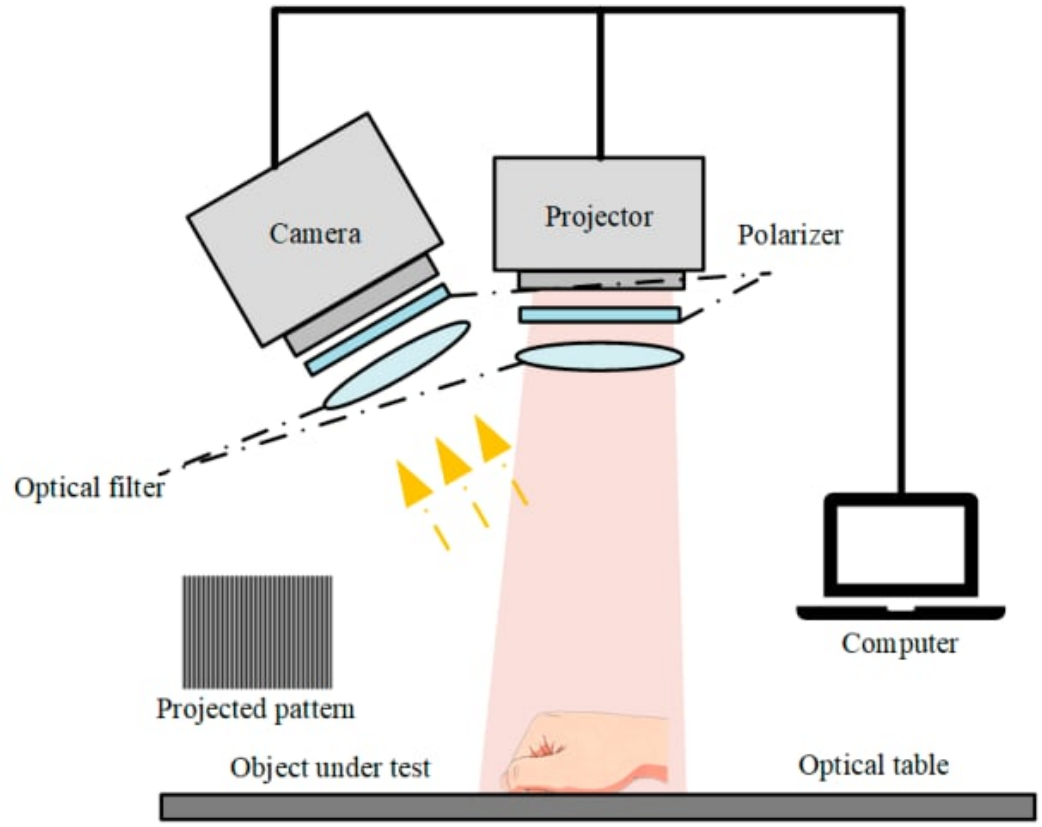

Figure 1. Schematic of the SFDI image acquisition system. The projector projects spatially modulated patterns onto the object under test, and the camera captures the reflected light.

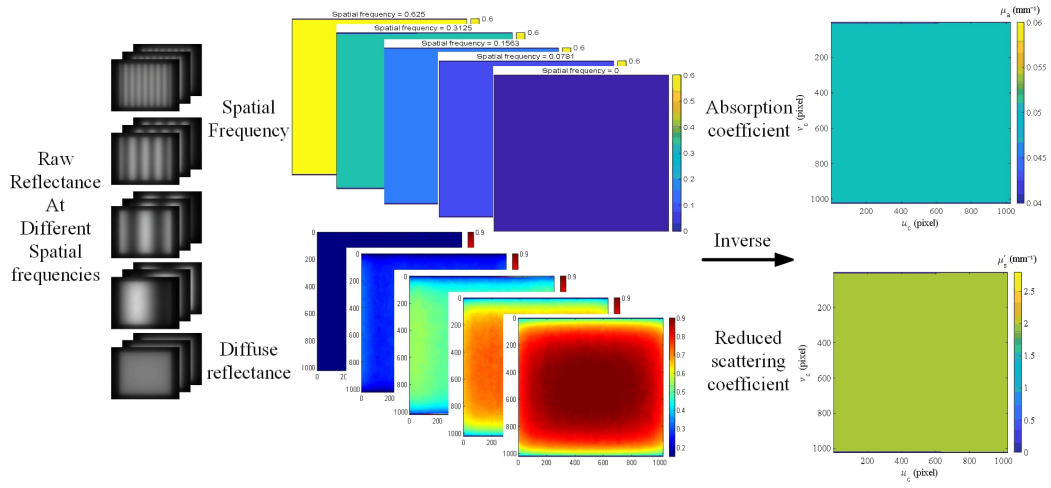

Figure 2. Data flow for SFDI optical property extraction. Raw images are demodulated and calibrated to obtain spatial-frequency-dependent diffuse reflectance, which is then inverted to yield maps of μ_a and μ'_s

Conventional SFDI systems typically project two spatial frequencies at a single wavelength onto planar or near-planar samples to retrieve optical properties from diffuse reflectance, using one zero-frequency (DC) and one high-frequency (AC) component. How-

ever, a single frequency can be ambiguous, and multi-frequency measurements reduce inversion error by providing richer information about tissue optical properties [15]. Yet the computational cost of multi-frequency inversion grows rapidly with the number of frequencies, particularly for least-squares fitting and look-up table methods, which can require hours of computation and hinder clinical translation and further development of multi-frequency SFDI.

Moreover, most existing deep learning approaches for optical property inversion rely on large ground-truth datasets for training [16,17] to optimize network weights and biases. Such training is time-consuming and costly, and the resulting networks are prone to overfitting, limiting their generalization to unseen scenarios [18]. In SFDI of biological tissue, obtaining sufficiently large and diverse ground-truth datasets experimentally is particularly challenging, especially in research settings. In contrast, untrained deep learning networks optimize the network parameter space by minimizing a loss function constructed primarily from the diffusion approximation. Because the selected physical model is grounded in the underlying physics, the network parameter space can be optimized without a training dataset, in contrast to supervised deep learning. Here, "untrained" means that no dataset-based pre-training is performed; the network weights are optimized for each input measurement. Although USFDI shares the physics-informed philosophy with conventional physics-informed neural networks (PINNs) [19], it is not a conventional PINN: the physical constraint is imposed through an analytical forward-model data-fidelity loss rather than a PDE residual, and the network operates on measured multi-frequency images rather than on coordinate inputs. A detailed comparison is given in Section 2.3.

Monte Carlo simulation has been combined with SFDI to compute diffuse reflectance [20–23]. In particular, the open-source software Blender has been integrated with SFDI [24,25], and synthetic datasets generated from Blender have shown promise for training deep learning models. Such approaches are low-cost and adaptable to diverse scenarios. In Blender, light transport through a material is simulated via 3D modeling and node-based rendering: surface nodes provide the 3D geometry, while volume nodes yield diffuse reflectance. When combined with 3D structured light measurement, this enables spatial frequency calibration on sample surfaces and thus optical property measurement for samples whose contours differ from the reference. In this study, Blender was used to generate simulated data to evaluate the proposed untrained framework, rather than for training.

In this work, we developed an untrained, physics-informed deep learning network for optical property inversion. The network is based on an improved U-Net with an encoder–decoder architecture. It takes as input 10-channel images formed by concatenating diffuse reflectance matrices measured at multiple spatial frequencies with the corresponding spatial frequency matrices (five channels each) and directly outputs a two-channel matrix of μ_a and μ'_s. By embedding the diffusion model into the loss function, the network eliminates the need for ground-truth training data. We validated the proposed method via simulations, phantom experiments, and in vivo measurements. Compared with least-squares fitting, our approach reduced the multi-frequency inversion time from over twenty minutes to under two minutes (approximately an 11-fold speedup) while maintaining high inversion accuracy.

2. Principle and Methods

2.1. Experimental SFDI System

The custom-built experimental SFDI system is primarily composed of two optical paths: the illumination path and the imaging path, as shown in Figure 3. In the illumination path, a digital micromirror device (DMD)-based projector (DLP4710EVM-LC, resolution

1920 × 1080, micromirror pitch 5.4 μm; Texas Instruments, Dallas, TX, USA) is used as the core structured light source. It is controlled by a computer to generate sinusoidal fringe patterns with specific spatial frequencies and phases. The projected beam passes through a linear polarizer (Daheng GCL-050004, Daheng Optics, Beijing, China) and obliquely illuminates the sample under test. In the imaging path, the diffusely reflected light from the sample passes through a narrow-band filter (Daheng GCC-300, center wavelength 630 nm, Daheng Optics, Beijing, China) and an analyzer. Here, the crossed polarizers are used to suppress specular reflection artifacts from the sample surface, while the narrow-band filter eliminates ambient light interference to improve the signal-to-noise ratio. Finally, the optical signal is captured by an industrial camera (Hikrobot MV-CS050-60UM, Hikrobot, Hangzhou, China). To achieve high-frame-rate acquisition and strict projection-acquisition synchronization, the camera frame is cropped to 1624 × 1236 to match the projection frequency, and its exposure is precisely controlled by an external hardware trigger signal output from the projector.

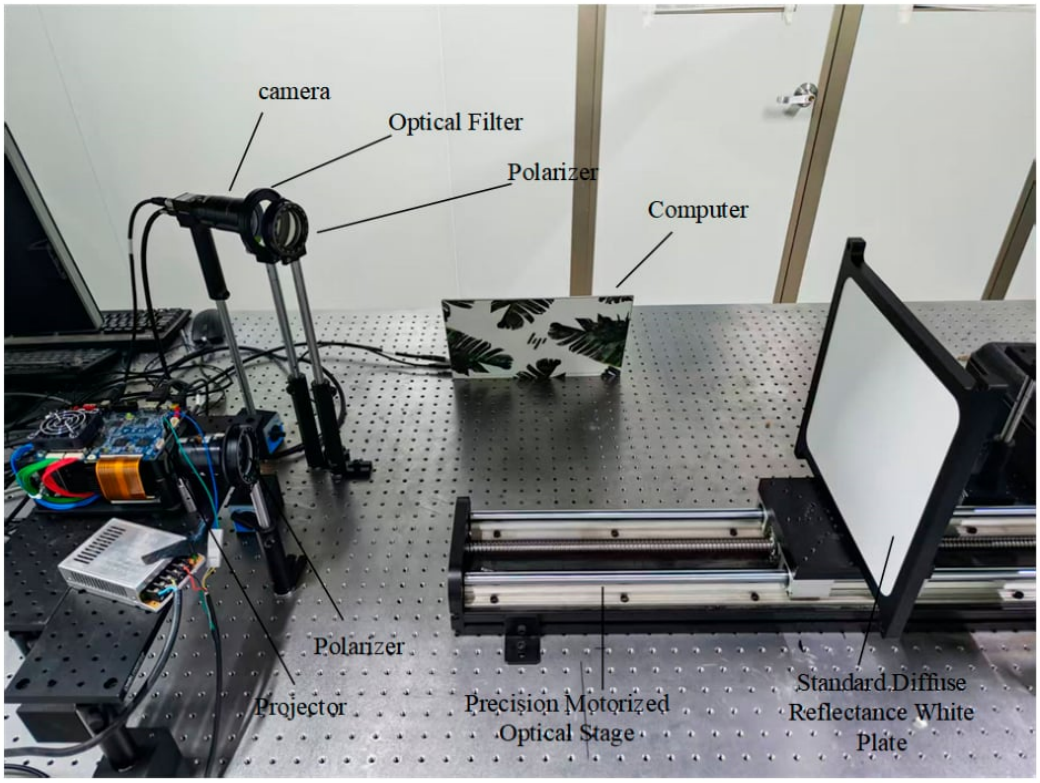

Figure 3. Photograph of the experimental SFDI system. The system consists of a projector, a camera, a polarizer, an optical filter, a precision motorized optical stage, a standard diffuse reflectance white plate, and a computer.

2.2. Diffusion-Approximation Model for SFDI

The diffusion approximation provides an analytical forward model for light transport in turbid media under spatially modulated illumination [26]. For a semi-infinite homogeneous medium, the diffuse reflectance R_d at a spatial frequency f_x can be expressed as

$$R(f_x) = \frac{3Aa'}{\left(\frac{\mu'_{eff}}{\mu_{tr}} + 1\right)\left(\frac{\mu'_{eff}}{\mu_{tr}} + 3A\right)} \quad (1)$$

where A is a medium-dependent coefficient given by

$$A = \frac{1 - R_{eff}}{2\left(1 + R_{eff}\right)} \tag{2}$$

where the effective reflection coefficient R_{eff} is given by

$$R_{eff} \approx 0.0636n + 0.668 + \frac{0.710}{n} - \frac{1.440}{n^2} \tag{3}$$

where n is the refractive index of the sample under test. The relative refractive index a' is given by

$$a' = \frac{\mu'_s}{\mu_{tr}} \tag{4}$$

where $\mu_{tr} = \mu_a + \mu'_s$, the effective attenuation coefficient μ'_{eff} is given by

$$\mu'_{eff} = \left[\mu_{eff}^2 + (2\pi f_x)^2\right]^{\frac{1}{2}} \tag{5}$$

where f_x is the spatial frequency of the fringe pattern on the sample surface and μ_{eff} is the effective attenuation coefficient, given by

$$\mu_{eff} = \sqrt{3\mu_a\left(\mu_a + \mu'_s\right)} \tag{6}$$

In Equation (5), f_x is the spatial frequency of the fringe pattern on the sample surface. To ensure the validity of the diffusion approximation in SFDI, the spatial frequency must satisfy a strict low-frequency condition. While $f_x < \mu_{tr}$ is often used as a rough criterion, the classical literature [27] suggests a more rigorous condition of $f_x \leq (0.25\sim0.33)\mu_{tr}$ to maintain high model accuracy.

In this study, to extract comprehensive optical information across multiple frequencies, the spatial frequency range was moderately extended. It should be noted that in our phantom experiment, the phantom has $\mu_{tr} = \mu_a + \mu'_s \approx 1.38\ \text{mm}^{-1}$, and the highest spatial frequency of $f_x = 0.625\ \text{mm}^{-1}$ corresponds to approximately $0.45\mu_{tr}$, which slightly exceeds this strict bound. However, the remaining four frequencies strictly satisfy the condition. Because the physics-informed network jointly optimizes the solution across all frequencies and applies soft constraints to mitigate model mismatches, the inversion remains robust. The selection and optimization of spatial frequency ranges for multi-frequency SFDI will be further investigated in our future work.

The diffusion approximation fundamentally assumes that scattering dominates over absorption ($\mu'_s \gg \mu_a$), which generally holds true for biological tissues where absorption is relatively low. However, if the tissue exhibits extremely high absorption, the diffusion model may lose validity, and the low-frequency condition $f_x < \mu_{tr}$ imposes an implicit minimum requirement for the effective attenuation coefficient to maintain a valid diffuse field. To mitigate the impact of potential model mismatches in such extreme cases, the physiological boundaries in our framework are implemented as soft constraints (i.e., L_{range} and L_{ratio} in Equation (13)) rather than hard limits. If the true optical properties fall outside these predefined ranges, the network will still output an inversion based on the dominant physics loss, though with a predictable decrease in accuracy. This degradation is acceptable and rarely occurs in standard biological measurements. Moreover, these soft constraint ranges can be flexibly adjusted in the loss function to accommodate specific high-absorption scenarios.

Because a single spatial frequency can correspond to multiple possible pairs of μ_a and μ'_s, multi-frequency measurements provide richer information and reduce the ambiguity of optical property inversion [15]. In this work, the diffusion-approximation model in Equations (1)–(6) serves as the physical forward model. It is scene-independent and therefore can be embedded into an untrained deep learning framework as a physical loss term,

enabling optical property inversion without ground-truth training data. It should be noted that Equations (1)–(6) are derived under the assumption of a homogeneous, semi-infinite, planar medium. When the sample is heterogeneous or curved—as in the human hand dorsum and palm—this analytical forward model may introduce model mismatch and reduce the inversion accuracy. Tissue heterogeneity violates the homogeneous-medium assumption, while surface curvature violates the planar boundary condition and distorts the local projection frequency and incidence geometry, leading to spatially varying model mismatch, especially near edges and high-curvature regions. In the proposed framework, these limitations are partially mitigated by the complementary regularization terms described in Section 2.4 and by the joint use of multiple spatial frequencies, which constrain the solution toward spatially smooth and physically plausible values. Nevertheless, the in vivo measurements on the hand and palm are intended as a feasibility demonstration rather than a quantitative validation on curved heterogeneous tissues. A systematic extension to such tissues, together with profile- or curvature-correction strategies, will be addressed in future work.

2.3. Untrained Physics-Informed U-Net

We developed an untrained, physics-informed deep learning network for optical property inversion. The network is based on an improved U-Net with an encoder–decoder architecture (Figure 4). It takes as input a 10-channel image formed by concatenating diffuse reflectance matrices measured at multiple spatial frequencies with the corresponding spatial frequency matrices (five channels each). The network directly outputs a two-channel matrix of the absorption coefficient μ_a and the reduced scattering coefficient μ'_s. Unlike supervised deep learning, the network requires no prior training. Instead, the loss function is constructed from a scene-independent physical model, and the network parameters are iteratively optimized for each input through the interaction between the network and the physical model. It should be emphasized that USFDI is not a conventional PINN. A conventional PINN typically represents the solution with a coordinate-based multilayer perceptron and minimizes PDE residuals at collocation points. In contrast, USFDI is an image-to-image network conditioned on measured multi-frequency reflectance. Its physics loss is computed by substituting the predicted μ_a and μ'_s maps into the analytical diffusion-approximation forward model, i.e., Equations (1)–(6), to generate theoretical diffuse reflectance, which is then compared with the measured multi-frequency reflectance. No PDE residual or collocation points are used. The U-Net is not claimed to be a fundamentally new backbone; its convolutional inductive bias, multi-scale feature extraction, and skip connections are used because they are appropriate for dense 1024 × 1024 image-to-image mapping and provide spatial regularization across pixels, which is difficult to achieve efficiently with a conventional coordinate-based MLP. The novelty of USFDI therefore lies in the untrained, image-domain, multi-frequency physics-informed formulation and the associated loss design rather than in the U-Net architecture alone.

The encoder contains three successive downsampling stages. The first stage applies two consecutive 3 × 3 convolution–batch normalization–ReLU blocks to extract features at the original 1024 × 1024 resolution, with 32 channels. Each subsequent stage first applies a 2 × 2 max pooling layer to halve the spatial resolution, followed by two consecutive 3 × 3 convolution–batch normalization–ReLU blocks, doubling the channel count to 64 and 128, respectively. After the third downsampling, a bottleneck layer consisting of two 3 × 3 convolutional blocks operates at a resolution of 128 × 128 with 256 channels, extracting the most high-level semantic features.

The decoder mirrors the encoder with three upsampling stages. Each stage uses a 2 ×2 transposed convolution with a stride of 2 to double the spatial resolution. Through skip

connections, the upsampled feature map is concatenated along the channel dimension with the corresponding feature map from the encoder. Then, two consecutive 3 × 3 convolutional blocks fuse these features. The channel count decreases to 128, 64, and 32 across the stages, and the resolution is finally restored to 1024 × 1024.

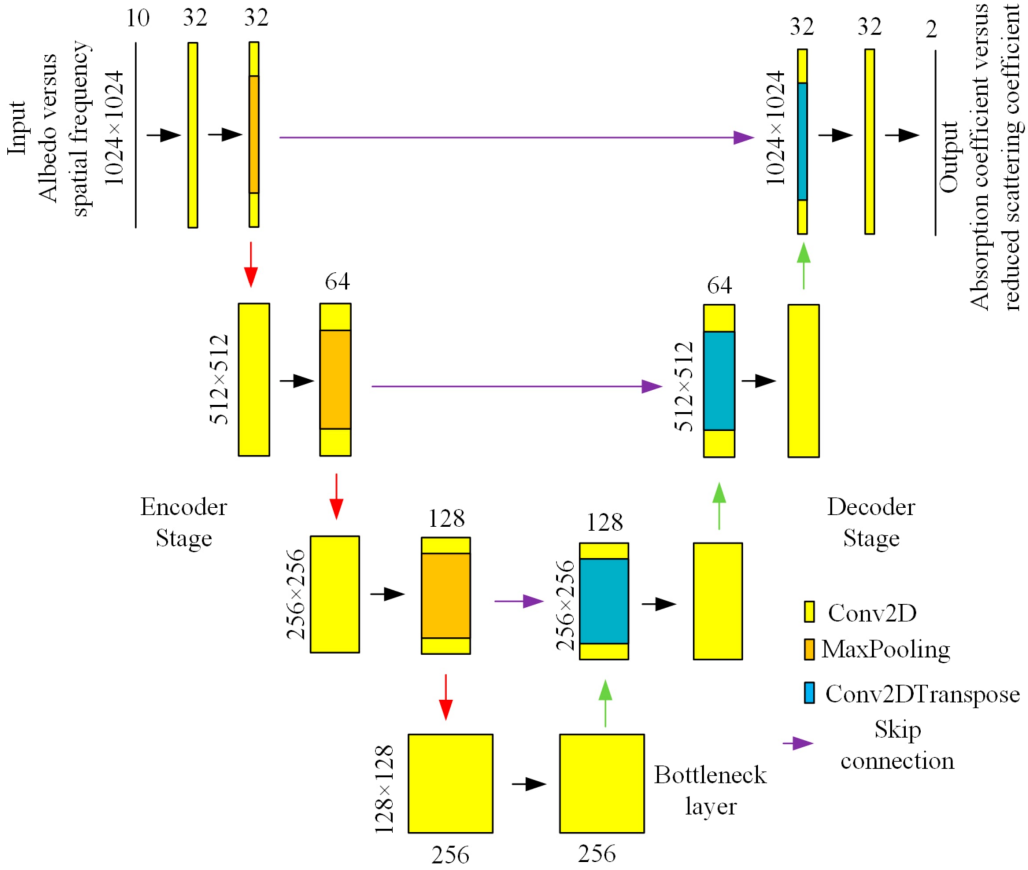

Figure 4. Architecture of the improved U-Net for untrained optical property inversion. The network consists of three main parts: the Encoder Stage, the Bottleneck layer, and the Decoder Stage. The input consists of 10 channels: five diffuse reflectance matrices and five corresponding spatial frequency matrices. The Encoder Stage utilizes Conv2D and MaxPooling blocks to extract multi-scale features, while the Decoder Stage employs Conv2DTranspose and skip connections to restore spatial resolution. The specific functions of each block are indicated in the legend. The output is a two-channel map of the absorption coefficient μ_a and the reduced scattering coefficient μ'_s

Finally, a 1 × 1 convolution maps the feature maps to a two-channel output corresponding to μ_a and μ'_s. A Softplus activation is applied at the output layer to enforce non-negativity, consistent with the physical constraints of optical properties. The total number of parameters in the network is 1,933,282, of which 1,930,466 are trainable.

During optimization, the network and the physical model are coupled: the network forward pass outputs the optical properties, and the loss function evaluates the deviation between the diffuse reflectance predicted by the physical model and the target diffuse reflectance. Gradients are then back-propagated to iteratively update the network weights. The input–output relationship is given by

$$[\mu_a, \mu'_s] = F_\theta(x) \tag{7}$$

where x is the input, θ denotes all network weights, and F_θ represents the nonlinear transformation defined by the network architecture. The output-layer weights directly determine μ_a

and μ'_s, whereas the preceding layers extract useful features from the input. Optimization iteratively adjusts these weights.

.

We used the Adam optimizer with an initial learning rate of 1.0×10^{-3} and a cosine annealing schedule. To balance computational efficiency and numerical stability, all computations were performed in float32 precision, and clipping and a small constant were introduced into the loss function to prevent numerical overflow.

2.4. Loss Functions

The loss function consists of five terms. First, a physics-based loss provides the foundation for the remaining constraints. A diffusion-approximation-based physical model loss (logarithmic error) substitutes the predicted absorption coefficient μ_a and reduced scattering coefficient μ'_s at low spatial frequencies into the forward model to compute the theoretical diffuse reflectance $\hat{R}_{d,i}$, which is then compared with the measured diffuse reflectance $R_{d,i}^{meas}$ via a logarithmic error. Multi-frequency constraints substantially improve the uniqueness and stability of the inversion. The logarithmic error treats large and small values equally, focusing on relative rather than absolute deviation, which is particularly important given the wide dynamic range of R_d across spatial frequencies in this study. The physics-based loss is given by

$$L_{phys} = \alpha \cdot \frac{1}{N_f} \sum_{i=1}^{N_f} \frac{1}{N_i} \sum_{p \in \Omega_{valid,i}} \left[Ln\left(\hat{R}_{d,i}(p) + \varepsilon\right) - Ln\left(R_{d,i}^{meas}(p) + \varepsilon\right) \right]^2 \quad (8)$$

Here L_{phys} denotes the physical model loss, $N_f = 5$ is the number of spatial frequencies, N_i is the number of valid pixels in the i-th frequency channel, and $\Omega_{valid,i}$ is the corresponding set of valid pixels. This design ensures that the network optimizes a solution (μ_a, μ'_s) consistent across all frequencies, rather than fitting well only at certain frequencies. $\varepsilon = 10^{-5}$ is a numerical stability constant, $\alpha = 0.1$ is a scaling factor, and p denotes the pixel position.

Second, a smoothness constraint suppresses noise and promotes spatial continuity in the optical property maps, avoiding unrealistic abrupt changes. It is expressed as the mean of the first-order differences of and along the horizontal and vertical directions, respectively.

$$L_{smooth} = \frac{1}{N_{valid}} \sum_{p \in \Omega_{valid}} \left(|\nabla_x \mu_a(p)| + \left|\nabla_y \mu_a(p)\right| + \left|\nabla_x \mu'_s(p)\right| + \left|\nabla_y \mu'_s(p)\right| \right) \quad (9)$$

where L_{smooth} denotes the smoothness loss, ∇_x and ∇_y denote the first-order differences along the horizontal and vertical directions, respectively, and N_{valid} is the cardinality of the union of valid pixels across all frequencies.

The smoothness loss, together with the range constraint, ensures spatial plausibility. Range regularization constrains the predicted absorption μ_a and reduced scattering coefficients μ'_s within physically plausible bounds. For each coefficient, penalties are imposed for values below the lower bound and above the upper bound, and these penalties are squared so that they increase with the magnitude of deviation. This range regularization term is given by

$$L_{range} = \frac{1}{N_{valid}} \sum_{p \in \Omega_{valid}} \begin{bmatrix} \left(\max\left(0, \mu_a^{\min} - \mu_a(p)\right)\right)^2 + \left(\max\left(0, \mu_a(p) - \mu_a^{\max}\right)\right)^2 \\ + \left(\max\left(0, \mu_s'^{\min} - \mu'_s(p)\right)\right)^2 + \left(\max\left(0, \mu'_s(p) - \mu_s'^{\max}\right)\right)^2 \end{bmatrix} \quad (10)$$

where L_{range} denotes the range loss, and $\mu_a^{\min}$, $\mu_a^{\max}$, $\mu_s'^{\min}$, and $\mu_s'^{\max}$ are the predefined lower and upper bounds for the absorption and reduced scattering coefficients, respectively. Specifically, in this study, the predefined bounds were set to $[0.01, 0.5]$ mm^{-1} for μ_a and $[0.5, 5.0]$ mm^{-1} for μ'_s, which are sufficiently wide to cover typical biological tissue optical

properties and are significantly broader than the ground-truth values used in our validations. It should be noted that this range regularization serves as a soft constraint through the quadratic penalty, rather than a hard boundary. This design ensures that the network optimizes towards physically plausible solutions without artificially forcing the accuracy. Furthermore, these bounds can be dynamically adjusted for specific measurement scenarios where the target optical properties are known to differ from the general range.

The range constraint ensures numerical plausibility by confining the predicted values to the range of biological tissues. Together with the logarithmic ratio loss, it further ensures physical plausibility. The bidirectional logarithmic ratio constraint restricts the ratio of the reduced scattering coefficient to the absorption coefficient within a plausible interval. This bidirectional constraint prevents the ratio from becoming either too large or too small, and the logarithmic form yields well-behaved gradients during back-propagation. This term is given by

$$L_{ratio} = \frac{1}{N_{valid}} \sum_{p \in \Omega_{valid}} \left[\left(\max\left(0, 1 - \log_{10} \frac{\mu'_s(p)}{\mu_a(p)}\right)\right)^2 + \left(\max\left(0, \log_{10} \frac{\mu'_s(p)}{\mu_a(p)} - 3\right)\right)^2 \right] \quad (11)$$

The bidirectional logarithmic ratio loss is consistent with the physical prior that the reduced scattering coefficient is much larger than the absorption coefficient, thereby assisting the physics-based loss in yielding a more plausible solution.

Finally, an R_d range constraint ensures that the predicted R_d values remain within the valid range of the measured data.

$$L_{rdrange} = \frac{1}{N_f} \sum_{i=1}^{N_f} \frac{1}{N_i} \sum_{p \in \Omega_{valid,i}} \left[\max\left(0, R_{d,i}^{\min} - \hat{R}_{d,i}(p)\right) + \max\left(0, \hat{R}_{d,i}(p) - R_{d,i}^{\max}\right) \right] \quad (12)$$

where $L_{rdrange}$ denotes the diffuse reflectance range loss, and $R_{d,i}^{\min}$ and $R_{d,i}^{\max}$ are the minimum and maximum values among all valid values in the i-th frequency channel, respectively. The total loss function is the weighted sum of the above terms:

$$L_{total} = \lambda_{phys} L_{phys} + \lambda_{smooth} L_{smooth} + \lambda_{range} L_{range} + \lambda_{ratio} L_{ratio} + \lambda_{rdrange} L_{rdrange} \quad (13)$$

The weights in Equation (13) were determined by a coordinate-wise (one-factor-at-a-time) tuning strategy on validation data with known ground truth (Blender-simulated samples). Specifically, all other weights were fixed while one weight was varied over a predefined range. For each candidate weight, the inversion accuracy was evaluated against the ground truth using the mean relative error of μ_a and μ'_s, and the convergence stability was also examined. The weight yielding the lowest combined inversion error while maintaining stable convergence was selected. This procedure was repeated for each loss term. The resulting weights were then fixed for all subsequent simulations, phantom experiments, and in vivo measurements; no in vivo data were used for tuning. The weights of the loss terms were therefore set to $\lambda_{phys} = 0.997$, $\lambda_{smooth} = 0.006$, $\lambda_{range} = 0.0035$, $\lambda_{ratio} = 0.00074$, and $\lambda_{rdrange} = 0.004$. Because the network is untrained and physics-based, it requires no training set and is therefore not subject to overfitting. The physics-driven loss embeds the diffusion model directly into the loss function, ensuring that the network output carries clear physical meaning rather than being a black-box prediction. The weights are assigned according to the relative importance of each objective.

3. Results

In this section, the proposed untrained deep learning-based spatial frequency domain imaging (USFDI) method was evaluated through Blender simulations, phantom experiments, and in vivo measurements. Diffuse reflectance and spatial frequency datasets were

generated in Blender4.4.0 (Blender Foundation, Amsterdam, Netherlands) and processed in MATLAB. Five low spatial frequencies (0, 0.0781, 0.1563, 0.3125, and 0.625 mm^{-1}) and their corresponding diffuse reflectance matrices were used as inputs. The inversion accuracy was evaluated by absolute error (AE) and relative error (RE), and the computation time was compared with that of conventional least-squares fitting (LSS).

3.1. Simulation Validation: Comparison with Least-Squares Fitting

We first evaluated the inversion accuracy and computational efficiency of USFDI using Blender-generated data. A flat plane, a plane tilted by 5°, a spherical segment, and a cylindrical surface were selected for optical property inversion. The ground-truth optical properties were set to μ_a = 0.03, 0.05, 0.06, and 0.07 mm^{-1} and μ'_s = 2, 3, 3.6, and 4mm^{-1}, respectively. Five low spatial frequencies (0, 0.0781, 0.1563, 0.3125, and 0.625 mm^{-1}) and their corresponding diffuse reflectance matrices were used as inputs.

Figure 5 shows the comparison between the true values and the values inverted by USFDI for the four samples. For both μ_a and μ'_s, the inverted values closely track the ground truth. The relative errors are within 8.93%, 5.67%, 4.91%, and 0.32% for μ_a, and within 0.23%, 0.94%, 5.07%, and 4.91% for μ'_s across the four samples. These results demonstrate that the untrained physics-informed network provides highly accurate multi-frequency inversion under varying surface geometries.

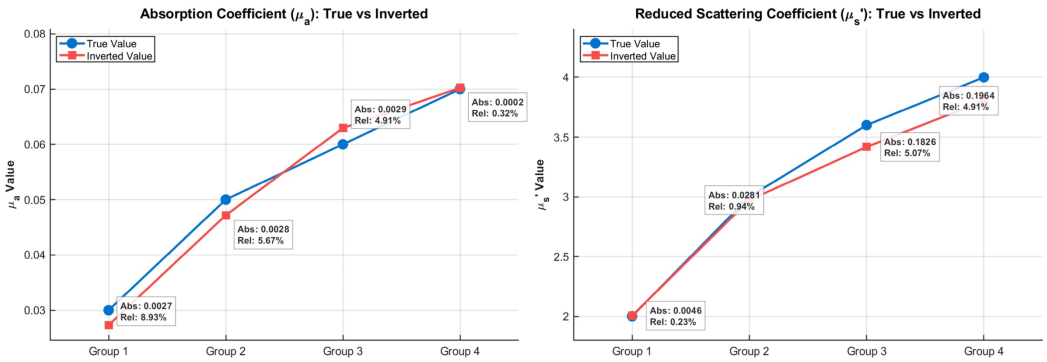

Figure 5. Comparison of inversion accuracy between the USFDI outputs and the ground-truth values set in Blender. The left and right panels show the absorption coefficient and the reduced scattering coefficient, respectively. Group 1, Group 2, Group 3, and Group 4 correspond to the flat plane, the plane tilted by 5°, the spherical segment, and the cylindrical surface, respectively. The ground-truth values are μ_a = 0.03, 0.05, 0.06, and 0.07mm^{-1} and μ'_s = 2,3, 3.6, and 4 mm^{-1} for the four groups.

Figure 6 shows the optical property maps retrieved by USFDI for the spherical sample. The left panel shows the Blender-rendered image, and the two right panels show the μ_a and μ'_s maps inverted by USFDI for the region outlined by the green box. The retrieved maps are spatially uniform and consistent with the ground-truth values.

To further justify the necessity of the multi-frequency input (five frequencies) and investigate the impact of frequency number on the inversion, we conducted a comparison using 2, 3, and 5 spatial frequencies. Figure 7 illustrates the relative errors of the inverted optical properties for the Blender-simulated sample (ground truth: μ_a = 0.06 mm^{-1} and μ'_s = 3.6 mm^{-1}).

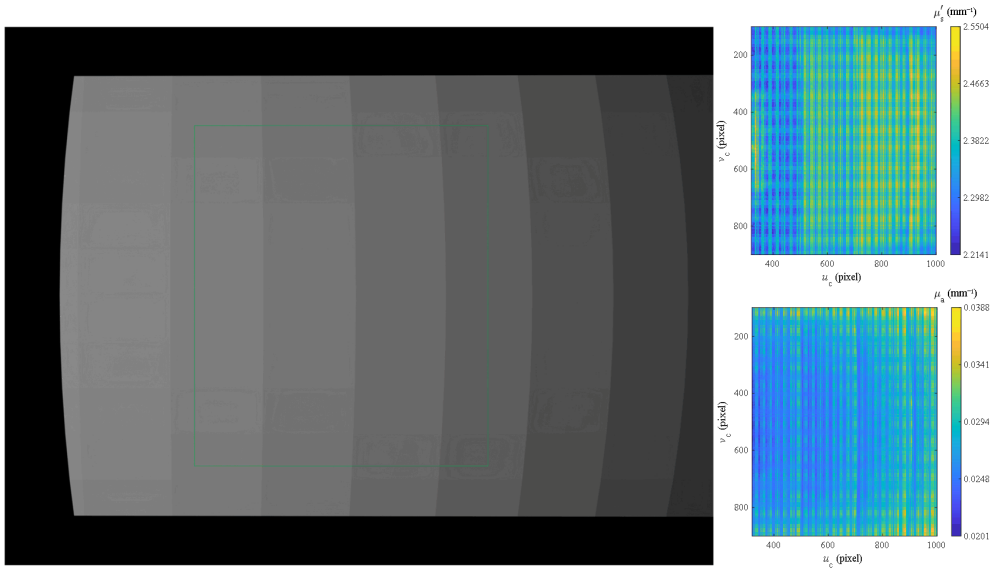

Figure 6. Blender-rendered spherical sample and optical property maps retrieved by USFDI. The left panel shows the Blender-rendered image. The two right panels show the μ_a and μ'_s maps inverted by USFDI for the region outlined by the green box in the left panel. The ground-truth values are $\mu_a = 0.03$ mm^{-1} and $\mu'_s = 2.4$ mm^{-1}.

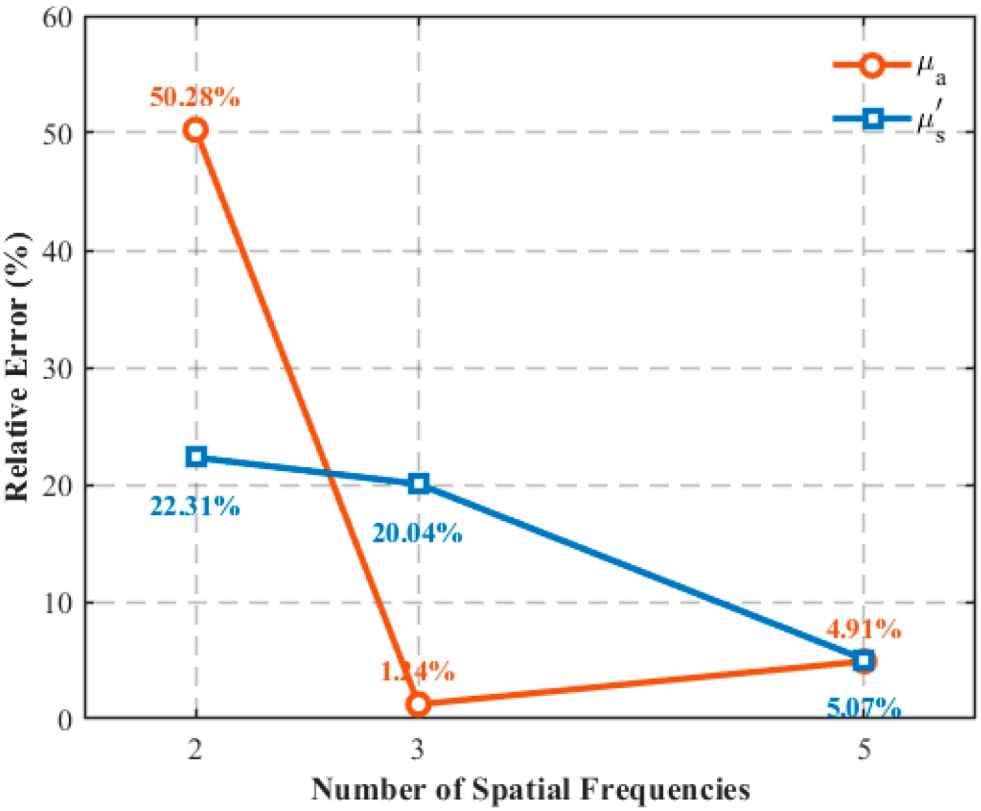

Figure 7. Optical property inversion performed using two, three, and five spatial frequencies. The relative errors for the absorption coefficient (μ_a) and reduced scattering coefficient (μ'_s) are shown. The ground-truth values are $\mu_a = 0.06$ mm^{-1} and $\mu'_s = 3.6$ mm^{-1}.

3.2. Ablation Study on Loss Terms

Before evaluating the contribution of the loss design, it is essential to analyze the residuals between the physics-based forward model and the actual measured data. Figure 8

presents the statistical distribution of relative residuals across the five spatial frequencies. Notably, the diffusion approximation (DA) model exhibits a systematic mismatch: it tends to underestimate the reflectance at low frequencies (0 and 0.0781 mm^{-1}) but overestimate it at the highest frequency (0.625 mm^{-1}). This phenomenon primarily originates from the inherent theoretical limitations of the DA model (e.g., the infinite-medium boundary assumption) and the multi-frequency compensation effect during joint optimization. Furthermore, the large standard deviations (error bars) indicate severe local fluctuations. This residual analysis confirms that relying solely on the physical forward model (as pixel-wise LSS does) will amplify these residuals into severe noise. Therefore, spatial regularization is necessary to constrain the solution space. To evaluate the contribution of the proposed regularization terms, we performed a system-level ablation. In the baseline variants, the physical forward model is retained to predict the diffuse reflectance, but the four designed regularization terms are removed, and the logarithmic data-fidelity metric is replaced by conventional mean absolute error (MAE) and mean squared error (MSE) metrics. This represents a standard unregularized optimization approach. In addition, to test the logarithmic physics loss alone, we removed the four regularization terms but retained the logarithmic physics loss (denoted as the "log-only" variant). Ten different sets of simulated data were inverted under these ablated settings, and the results were compared with those of the full USFDI. Figure 9 shows the reconstructed μ_a and μ'_s values against their ground truths. Panels (a)–(c) compare the inverted μ_a for fixed μ'_s = 2, 3, and 3.6 mm^{-1}, respectively, and panels (d)–(f) compare the inverted μ'_s for fixed μ_a = 0.03, 0.04, and 0.05 mm^{-1}, respectively.

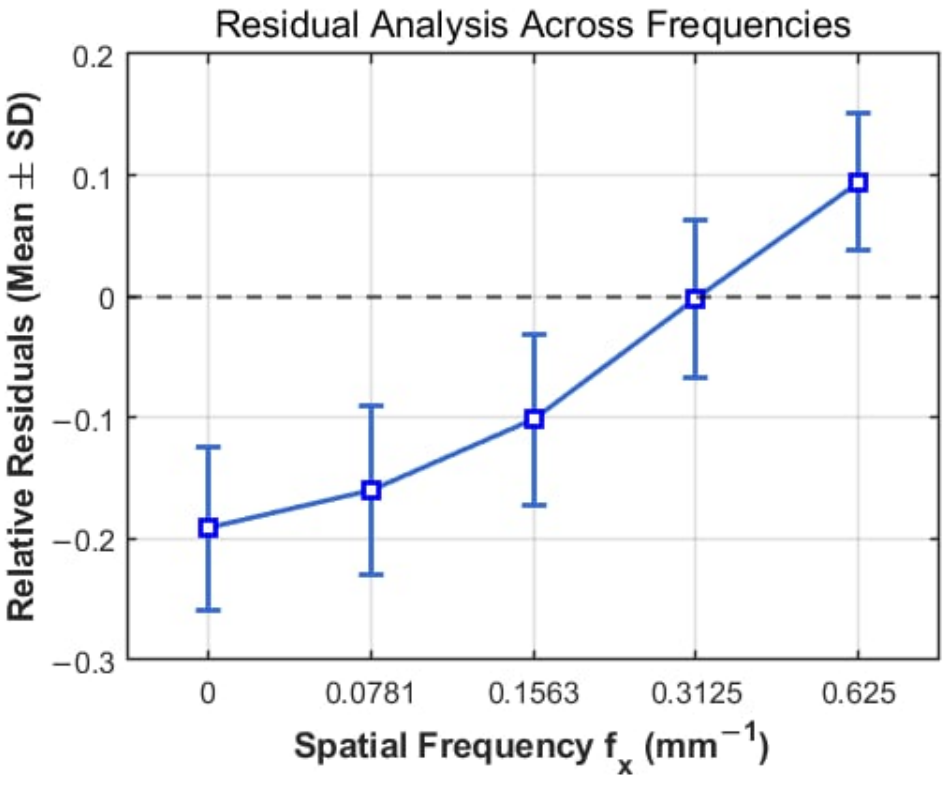

Figure 8. Statistical distribution of relative residuals $((R_{d,pred} - R_{d,meas})/R_{d,meas})$across different spatial frequencies. The markers represent the mean values, and the error bars indicate the standard deviations (SD) across all valid pixels. The systematic bias and large variance reveal the inherent limitations of the DA model, justifying the necessity of spatial priors (regularization) in USFDI.

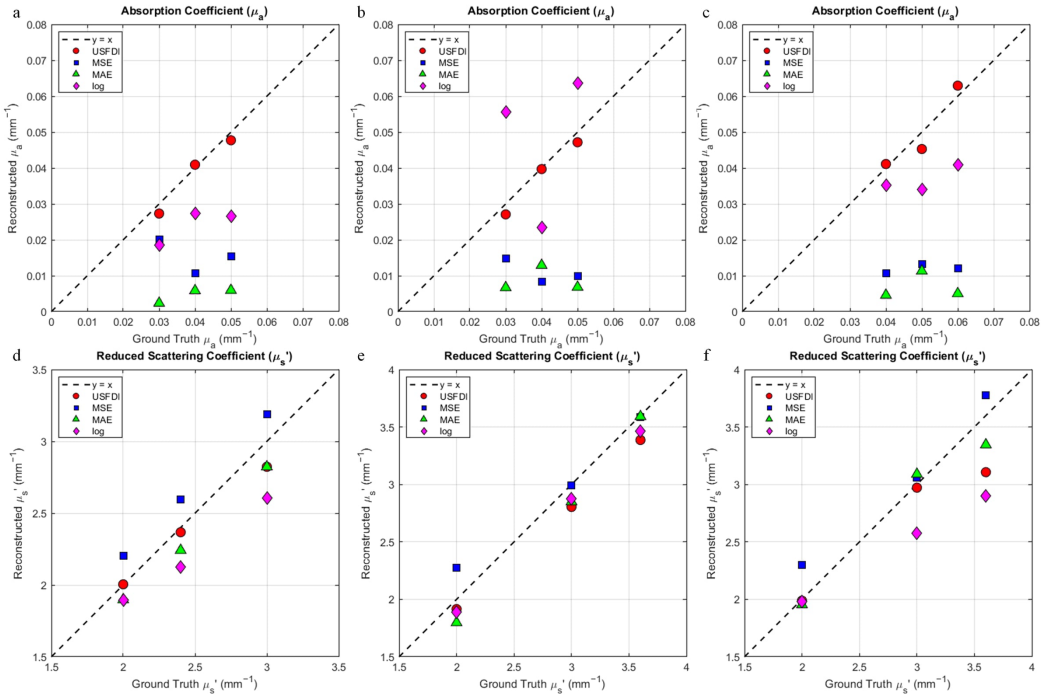

Figure 9. Ablation study on the proposed loss design. (**a**–**c**) Reconstructed μ_a versus ground truth for μ'_s = 2, 3, and 3.6 mm^{-1}, respectively. (**d**–**f**) Reconstructed μ'_s versus ground truth for μ_a = 0.03, 0.04, and 0.05 mm^{-1}, respectively. Red circles, blue squares, green triangles, and magenta diamonds denote the full USFDI, MSE baseline, MAE baseline, and the "Log-only" variant, respectively. The "Log-only" variant utilizes only the logarithmic physics loss without any regularization terms. The dashed line indicates y = x.

With MAE or MSE alone, the reconstructed values deviate noticeably from the ground-truth line, especially for μ_a, where the points are systematically underestimated. Similarly, the "log-only" variant (magenta diamonds) fails to accurately recover the optical properties, exhibiting large deviations from the ground truth. In contrast, the full USFDI yields reconstructed values that are closer to the ground truth for both coefficients.

3.3. Phantom Validation and Computational Cost Analysis

To evaluate the practical feasibility of USFDI, we performed phantom validation using a commercially available optical phantom with known optical properties. The inversion data flow for the phantom is illustrated in Figure 10, where the five spatial frequency matrices and the corresponding diffuse reflectance matrices are used as inputs to USFDI to obtain the μ_a and μ'_s maps. The ground-truth optical properties provided by the manufacturer were μ_a = 0.0376 mm^{-1} and μ'_s = 1.34 mm^{-1}. In a representative single inversion run, USFDI yielded μ_a = 0.0379 mm^{-1} and μ'_s = 1.5364 mm^{-1}. The absolute and relative errors were 0.0003 mm^{-1} and 0.79% for μ_a, and 0.1964 mm^{-1} and 14.65% for μ'_s, respectively. Therefore, to evaluate the statistical robustness of USFDI, we conducted five repeated independent experiments. the inverted values were 0.0413 ± 0.0022 mm^{-1} for μ_a and 1.4821 ± 0.0481 mm^{-1} for μ'_s, with average relative errors of approximately 10%, which is within a reasonable range.

To further evaluate the practical advantages and robustness of USFDI, we compared its inversion results with those obtained by conventional LSS on the same phantom dataset. To ensure a fair comparison, the USFDI results are presented as the mean of five repeated runs, whereas a single LSS run is presented because the LSS solver is deterministic under identical initializations and stopping criteria. Figure 11 presents a direct comparison of the inverted values. As shown in the bar chart, the mean values of USFDI (blue bars) are closer

to the ground truth (black dashed line) than those of LSS (orange bars) for both μ_a and μ'_s, indicating a higher overall inversion accuracy.

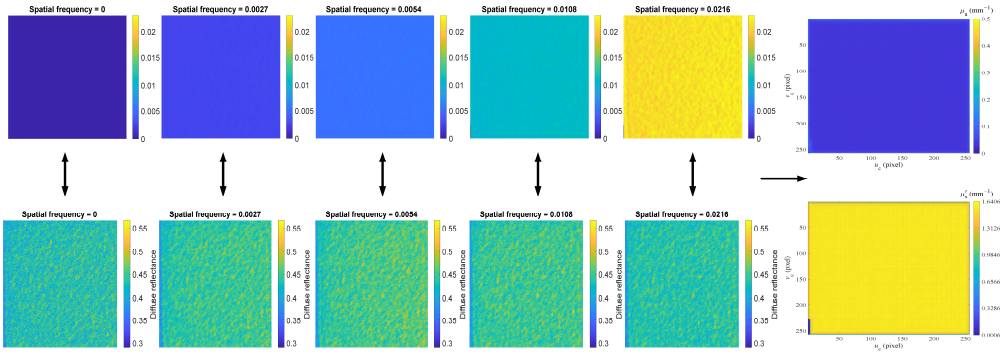

Figure 10. Schematic of optical property inversion for the phantom using USFDI. The five columns on the left show the input data: the top row shows the spatial frequency matrices at five spatial frequencies, and the bottom row shows the corresponding diffuse reflectance matrices. The double-headed arrows indicate the one-to-one correspondence between each spatial frequency and its diffuse reflectance. These paired inputs are fed into the USFDI network, which outputs the absorption coefficient μ_a and reduced scattering coefficient μ'_s maps shown on the right. The color bars denote the corresponding coefficient values in mm^{-1}.

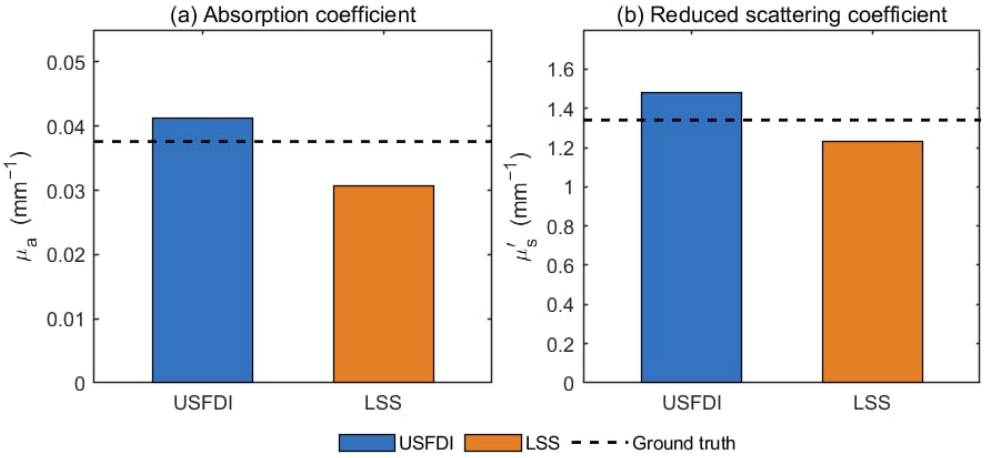

Figure 11. Comparison of inversion accuracy between USFDI and LSS for the phantom. (**a**) The absorption coefficient μ_a and (**b**) the reduced scattering coefficient μ'_s. The blue and orange bars represent the mean value of repeated USFDI inversions and the single LSS inversion result, respectively. The black dashed line indicates the ground-truth values provided by the manufacturer. The color bars denote the corresponding coefficient values in mm^{-1}.

Furthermore, Figure 12 illustrates the spatial distributions of the signed errors for both methods across the entire field of view. For all experiments, the optimization was run for a maximum of 300 epochs with an early-stopping patience of 50 epochs based on the monitored total loss; that is, optimization was terminated if the loss did not decrease for 50 consecutive epochs. In our experiments, the loss continued to decrease until the 300-epoch limit. These results demonstrate the practical feasibility of USFDI for phantom measurement.

Computational cost comparison. To evaluate the computational efficiency under a realistic wide-field setting, we compared the wall-clock time required to process a full 1024 × 1024 field of view (comprising 5 spatial-frequency matrices and 5 diffuse-reflectance matrices, totaling 10 arrays with over 10 million data points). All computations were performed on the same desktop workstation equipped with an NVIDIA RTX A6000 GPU (48 GB memory; NVIDIA Corporation, Santa Clara, CA, USA) and an Intel Xeon E5-2620 v4

CPU (8 physical cores, 2.10 GHz, 128 GB RAM; Intel Corporation, Santa Clara, CA, USA), using TensorFlow 2.10.0 (Google, Mountain View, CA, USA) and MATLAB R2022a (Parallel Computing Toolbox 7.6; MathWorks, Natick, MA, USA), respectively. The CPU-parallel least-squares fitting (LSS) used these identical inputs and was implemented in MATLAB R2022a using lsqnonlin with the default trust-region-reflective algorithm, lb = $[1 \times 10^{-6}, 1 \times 10^{-6}]$, ub = [10, 10], MaxFunctionEvaluations = 100, MaxIterations = 10, and MATLAB default tolerances (FunctionTolerance = 1×10^{-6}, StepTolerance = 1×10^{-6}); parallelized via parfor across 8 workers, it required 1254 s. In contrast, USFDI required only 107 s, corresponding to an approximately 11.7-fold wall-clock speed-up. Timing covered only the fitting/inference stage and excluded file I/O and pre/post-processing.

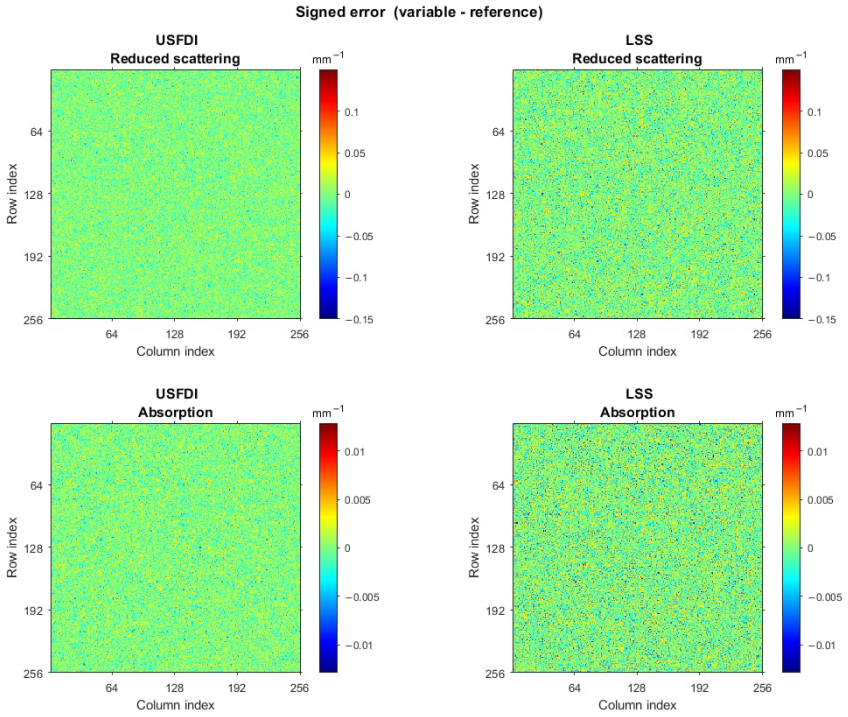

Figure 12. Spatial distributions of the signed errors (inverted value minus ground truth) for USFDI and LSS across the phantom region. The top and bottom rows show the error maps for the reduced scattering coefficient μ'_s and the absorption coefficient μ_a, respectively. The left and right columns display the results obtained by USFDI and LSS, respectively. The color bars denote the corresponding signed error values in mm^{-1}.

3.4. In Vivo Validation

3.4.1. Hand Dorsum and Constricted Finger

To evaluate the feasibility of USFDI for in vivo measurement, we first applied it to the human hand dorsum. Figure 13 shows the retrieved μ_a and μ'_s maps. The μ_a map clearly reveals the vascular distribution, whereas the μ'_s map is more spatially uniform.

We then constricted the index finger with a dark rubber band to alter the local blood distribution and avoid overexposure from a light-colored band. Figure 14 compares the optical property maps of the constricted index finger and the unbound fingers. Because the constriction changes the blood volume and distribution, the μ_a of the index finger differs from that of the other fingers. In contrast, the μ'_s of the index finger remains similar to that of the unbound fingers, since the constriction does not significantly alter the tissue structure.

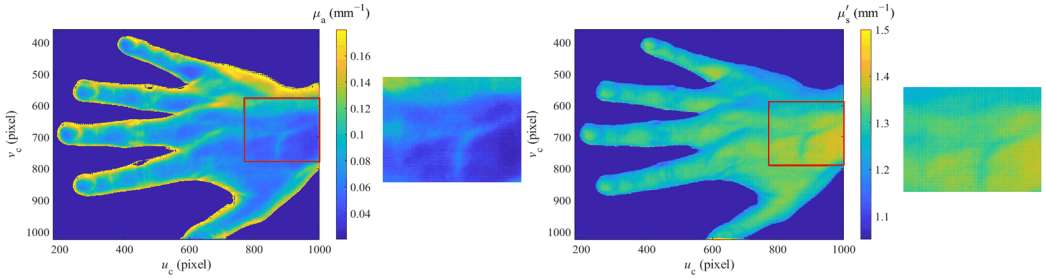

Figure 13. In vivo optical property maps of the hand dorsum retrieved by USFDI. The top and bottom panels show the μ_a and μ'_s maps, respectively. The insets show magnified views of the region outlined by the red box.

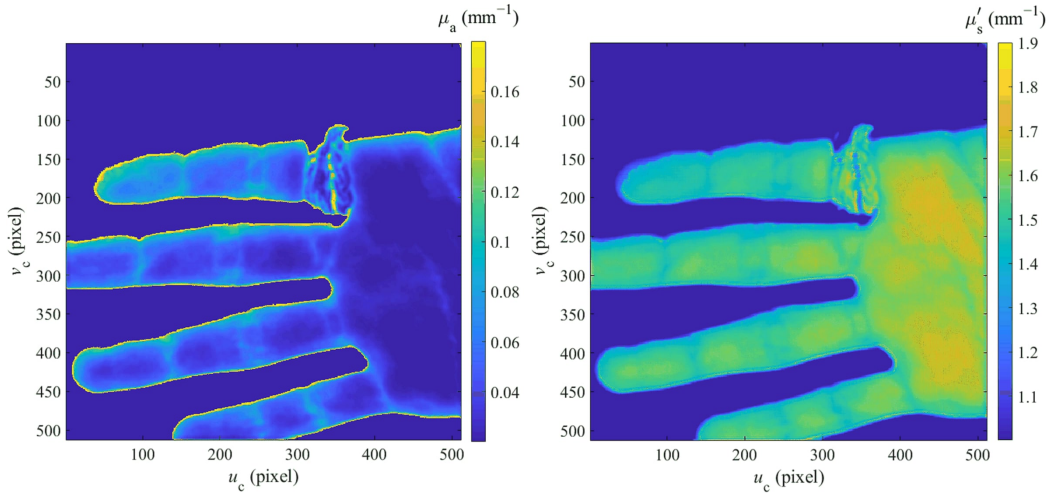

Figure 14. Comparison of in vivo optical property maps between the constricted index finger and the unbound fingers retrieved by USFDI. The left and right panels show the μ_a and μ'_s maps, respectively. The index finger was constricted with a dark rubber band to alter the local blood distribution.

3.4.2. Palm Under Dehydrated and Hydrated Conditions

To further validate USFDI under physiologically relevant but visually imperceptible changes, we measured the same palm under two hydration states. The subject first underwent 24 h of water deprivation, consuming only six boiled eggs (a high-protein diet to promote diuresis), after which the left palm was measured. The same palm was then measured again after 24 h of high water intake [28]. The changes in the palm during this period were imperceptible to both the naked eye and a camera.

Figure 15 shows the retrieved optical property maps. The top row shows the dehydrated state, and the bottom row shows the hydrated state. Averaged over the palm region, the dehydrated state yielded $\mu_a = 0.0682$ mm^{-1} and $\mu'_s = 2.4086$ mm^{-1}, whereas the hydrated state yielded $\mu_a = 0.0766$ mm^{-1} and $\mu'_s = 2.2486$ mm^{-1} for the same region. Both visual inspection and quantitative comparison show that dehydration decreases μ_a but increases μ'_s relative to the hydrated state.

These trends are phenomenologically consistent with physiological expectations. For the absorption coefficient (μ_a), physiological dehydration typically reduces microcirculatory blood volume and local hemoglobin content, which plausibly lowers the overall absorption at 630 nm. Although a single-wavelength measurement cannot definitively exclude concurrent changes from other chromophores (e.g., melanin concentration due to water loss), the observed decrease in μ_a is consistent with a dominant reduction in blood-related absorption.

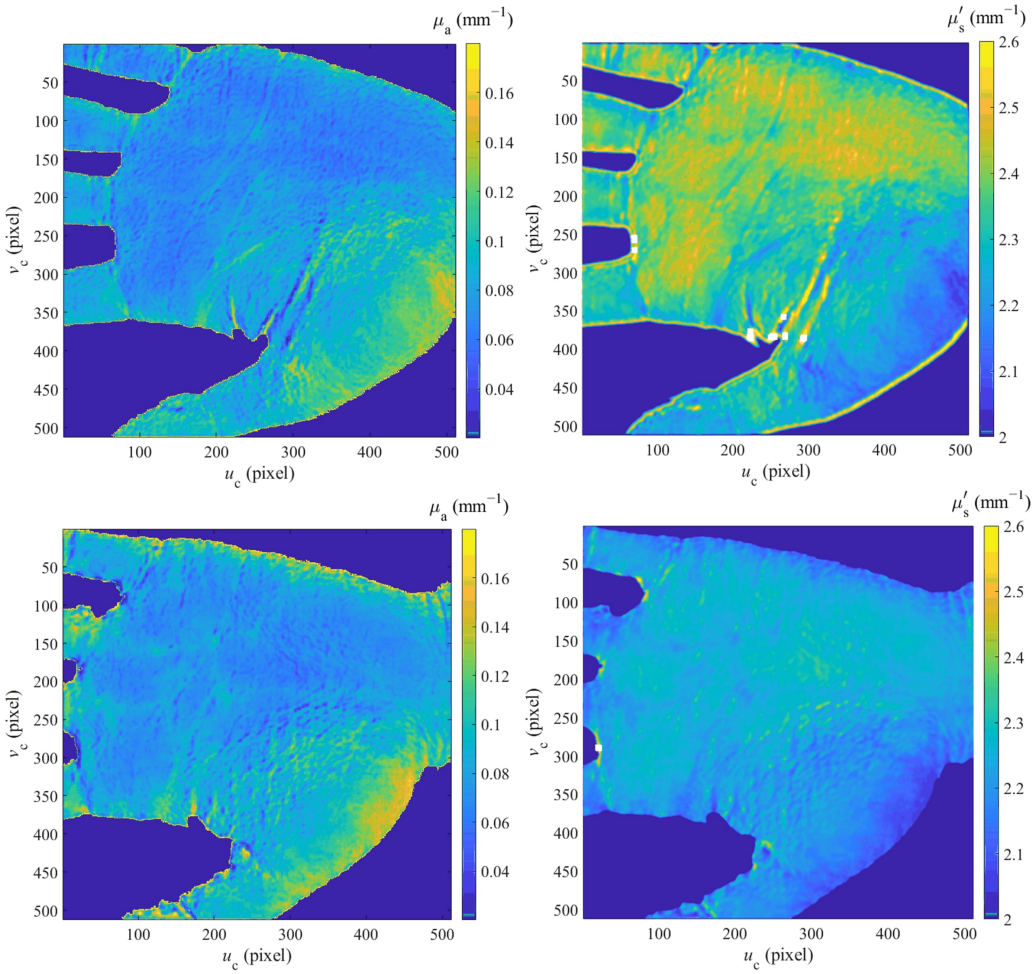

Figure 15. In vivo optical property maps of the palm under dehydrated and hydrated conditions retrieved by USFDI. The top and bottom rows show the dehydrated and hydrated states, respectively. The left and right columns show the μ_a and μ'_s maps, respectively.

For the reduced scattering coefficient (μ'_s), physiological dehydration mainly reduces extracellular and intracellular water, leading to mild tissue shrinkage, increased scatterer density, increased refractive-index mismatch, and possible changes in the anisotropy factor; these effects can plausibly increase μ'_s. In contrast, the ex vivo desiccation study in [28] involved extreme, structurally destructive dehydration, in which cellular structures collapse and scattering interfaces are largely lost, which can reduce μ'_s. Because the wavelength, tissue state, and measurement protocol differ, our in vivo result should not be directly compared with that ex vivo result.

Moreover, the present measurement involves a single subject, a fixed measurement order, a single wavelength (630 nm), and no independent gold-standard hydration measurement. Consequently, the observed opposing trends are interpreted as a proof-of-concept demonstration of relative physiological changes, rather than definitive absolute values validated against external physiological sensors. Thus, the hydration results (Figure 15) are presented only as an in vivo feasibility demonstration, not as a definitive physiological or clinical conclusion.

4. Discussion

4.1. Advantages of Multi-Frequency Constraints and Loss Function Design

To ensure the uniqueness and stability of the inversion, our network design utilizes 5 spatial frequencies. In conventional single-frequency SFDI, the ill-posed nature of the

inversion often leads to severe coupling between absorption and scattering. Our simulation results demonstrate this limitation: with only 2 frequencies (DC and the highest AC), the network fails to obtain sufficient information, resulting in large errors for both μ_a (50.28%) and μ'_s (22.31%). When the input is increased to 3 frequencies, the error for μ_a drops sharply to 1.41%, but μ'_s remains at 20.04%. This phenomenon occurs because μ_a and μ'_s are highly coupled, and 3 frequencies lack sufficient high-frequency constraints to decouple the scattering information. By employing 5 frequencies, the network gains richer spatial-frequency features, achieving the most balanced performance with errors of 4.91% for μ_a and 5.07% for μ'_s. Although the 3-frequency input yields a lower relative error for μ_a, its scattering inversion is highly unstable. Therefore, among the evaluated configurations, the 5-frequency setup provides a more balanced trade-off for the joint inversion of both parameters, validating our network design.

Furthermore, because μ_a and μ'_s are highly correlated and are jointly fitted from multi-frequency diffuse reflectance, our loss design prioritizes stabilizing both parameters within an acceptable error range rather than achieving absolute optimal accuracy for a single parameter alone. The ablation results demonstrate that the physics-based loss alone (even in logarithmic form) is insufficient to constrain the severely ill-posed solution. In contrast, the smoothness, range, bidirectional logarithmic ratio, and R_d range constraints jointly stabilize the optimization and guide the network toward physically plausible optical properties. Unlike supervised deep learning methods [16,17] that require massive, experimentally challenging ground-truth datasets and remain prone to overfitting, USFDI operates completely untrained on measured data. The loss function is constructed directly from the physical model, eliminating the domain gap between simulated training sets and real-world clinical measurements. It is crucial to distinguish USFDI from conventional Physics-Informed Neural Networks (PINNs) [19]. Traditional PINNs typically employ coordinate-based multi-layer perceptrons (MLPs) and minimize partial differential equation (PDE) residuals at collocation points. USFDI, however, is an image-to-image network conditioned on measured multi-frequency reflectance. Its physical constraint is imposed through an analytical forward-model data-fidelity loss rather than a PDE residual. The convolutional inductive bias of the U-Net provides essential spatial regularization across pixels. Therefore, the novelty of USFDI lies not in the U-Net architecture itself, but in this untrained, image-domain, multi-frequency physics-informed formulation.

4.2. Performance Comparison and Computational Efficiency Analysis

In simulation validation, Blender simulates light transport using the Monte Carlo (MC) method, whereas both USFDI and conventional least-squares fitting (LSS) rely on the Diffusion Approximation (DA) forward model. This inherent MC-DA model mismatch, particularly the absolute amplitude discrepancy at low spatial frequencies, prevents pixel-wise LSS from serving as a fair accuracy baseline. Therefore, we compared the USFDI outputs directly against the ground-truth values set in Blender. In phantom validation, the error maps of USFDI are notably smoother and more spatially uniform. In contrast, the LSS results exhibit more pronounced random noise and scattered high-error spots. This is because LSS performs strict pixel-by-pixel fitting, making it highly sensitive to measurement noise and minor model mismatches. The spatial regularization and physical constraints embedded in USFDI effectively suppress these random fluctuations, demonstrating that USFDI provides a more stable and homogeneous optical property mapping for practical measurements.

In terms of computational efficiency, the LSS baseline was deliberately implemented on a multi-core CPU rather than on the GPU. While GPU acceleration is natural for homogeneous tensor operations, mapping over one million independent per-pixel nonlinear least-squares problems onto GPU warps forces the abandonment of robust optimization

mechanisms (e.g., trust-region and line search). Consequently, a GPU-based LSS requires manual tuning of algorithmic parameters—such as damping factors, step clipping, and convergence thresholds—when adapting to different measurement scenarios and sample geometries. This extensive prior manual intervention leads to severe local-minimum collapse and accuracy degradation. In contrast, both the CPU-parallel lsqnonlin and our proposed USFDI require no such extensive manual parameter tuning. Furthermore, although look-up table (LUT) methods are established for fast inversion, they face inherent limitations in complex multifrequency scenarios. Mapping multiple spatial frequencies alongside 3D surface corrections for non-planar biological tissues leads to an exponential increase in table dimensionality. More importantly, LUTs are highly sensitive to the forward model, making them susceptible to the same MC-DA model mismatch. Therefore, the proposed USFDI bypasses the need for LUT generation and avoids the instability of GPU-based optimization, while naturally handling the MC-DA mismatch through physics-based soft constraints. Additionally, regarding the optimization process, because USFDI is untrained and optimized for each input, the optimization essentially acts as an iterative solver. A longer computation time allows more iterative updates of the network weights, enabling the predicted μ_a and μ'_s to better fit the diffusion-approximation forward model and the measured multi-frequency reflectance, thereby reducing the inversion error. However, the improvement exhibits diminishing marginal returns: the loss decreased rapidly during the first approximately 50 epochs and more slowly thereafter. Therefore, our early-stopping strategy (maximum 300 epochs with a patience of 50 epochs) provides a practical trade-off between inversion accuracy and computational efficiency.

4.3. Model Assumptions, Limitations, and Error Source Analysis

The differences between the measured values and the manufacturer-reported values can be attributed to several factors. The manufacturer-provided values are nominal values at specified measurement conditions and carry their own uncertainty, whereas our measurements were performed with our specific SFDI system, calibration procedure, and phantom boundary conditions. The observed differences therefore reflect a combination of phantom nominal uncertainty, measurement noise and calibration uncertainty, diffusion-approximation model mismatch, and the intrinsic coupling between μ_a and μ'_s. Furthermore, in the phantom experiment, the large difference in the absolute error magnitude between μ_a and μ'_s is primarily attributed to three factors: (i) the intrinsic scale difference; (ii) the physical sensitivity of the diffusion approximation, where diffuse reflectance is more sensitive to absorption changes; and (iii) the use of primarily low spatial frequencies, which favors μ_a sensitivity but provides relatively weaker constraints for μ'_s. It should be noted that due to the random initialization of network weights, GPU floating-point non-determinism, and the inherent coupling between μ_a and μ'_s, the inversion results exhibit slight run-to-run fluctuations.

Furthermore, the curved surface of the spherical phantom in the simulation violates the flat, semi-infinite boundary assumption of the diffusion approximation, and the local spatial frequency is distorted by the surface normal. These geometric mismatches inevitably introduce minor boundary artifacts in the retrieved maps. It should also be noted that the present phantom validation used a single homogeneous phantom with one nominal optical-property combination. It demonstrates the feasibility and relative advantage of USFDI under identical measurement conditions, rather than a comprehensive quantitative calibration over a broad μ_a/μ'_s range. Systematic validation using multiple homogeneous phantoms, as well as heterogeneous phantoms with inclusions and curved geometries, will be a major focus of future work.

4.4. Physiological Interpretation and Limitations of In Vivo Measurements

For the in vivo hand dorsum measurement, the spatial contrast in the μ_a map is consistent with vascular absorption. However, because the measurement was performed at a single wavelength (630 nm), this contrast cannot be uniquely attributed to hemoglobin; melanin and other chromophores may also contribute. Without an independent hemodynamic gold standard, these μ_a maps are interpreted as relative absorption contrast rather than absolute physiological quantification.

In the palm hydration experiment, the observed trends are phenomenologically consistent with physiological expectations. For the absorption coefficient (μ_a), physiological dehydration typically reduces microcirculatory blood volume and local hemoglobin content, which plausibly lowers the overall absorption at 630 nm. Although a single-wavelength measurement cannot definitively exclude concurrent changes from other chromophores, the observed decrease in μ_a is consistent with a dominant reduction in blood-related absorption. For the reduced scattering coefficient (μ'_s), physiological dehydration mainly reduces extracellular and intracellular water, leading to mild tissue shrinkage, increased scatterer density, and increased refractive-index mismatch; these effects can plausibly increase μ'_s. In contrast, the ex vivo desiccation study in [28] involved extreme, structurally destructive dehydration, which can reduce μ'_s. Because the wavelength, tissue state, and measurement protocol differ, our in vivo result should not be directly compared with that ex vivo result.

It should be noted that the absolute change in μ_a (0.0084 mm^{-1}) is nearly four times the standard deviation of our system's repeated measurements (0.0022 mm^{-1}). Although in vivo measurements may exhibit slightly higher variance due to subject motion, this margin suggests that the observed changes can be distinguished from instrumental noise to a certain extent. Furthermore, the opposing trends in μ_a and μ'_s (one decreasing, one increasing) strongly suggest a genuine physiological response, as typical instrumental drift would generally result in unidirectional changes. Nevertheless, we acknowledge that this is a proof-of-concept self-experiment with a fixed measurement order and lacks an independent gold-standard hydration sensor. Therefore, these results serve as an in vivo feasibility demonstration rather than a definitive clinical conclusion. Future studies with randomized crossover designs and larger cohorts are required to statistically validate these findings. Finally, the current forward model assumes a homogeneous semi-infinite medium; therefore, the multi-frequency measurements are used to reduce inversion ambiguity rather than to provide depth-resolved or layered characterization. Layered/multilayer forward models will be incorporated in future work for depth-sensitive optical property mapping.

5. Conclusions

In this work, we developed an untrained physics-informed deep learning framework, termed USFDI, for rapid multi-frequency optical property inversion in wide-field SFDI. By embedding a diffusion-approximation-based forward model into the loss function, the network requires no ground-truth training dataset and avoids the overfitting risk of conventional supervised networks. USFDI directly maps multi-frequency diffuse reflectance and spatial frequency inputs to paired maps of the absorption coefficient μ_a and the reduced scattering coefficient μ'_s.

In Blender simulations, USFDI was directly evaluated against the ground-truth optical properties, demonstrating high inversion accuracy. In physical phantom experiments, compared with least-squares fitting (LSS), USFDI exhibited superior inversion accuracy and better spatial stability. Furthermore, for a full 1024 × 1024 field of view, USFDI reduced the multifrequency inversion time from over twenty minutes to under two minutes, corresponding to an approximately 11-fold speedup. Phantom validation showed average relative errors of approximately 10%, and in vivo measurements of the hand dorsum, constricted

finger, and palm under dehydrated and hydrated conditions produced physiologically plausible relative trends. Although these in vivo results establish technical feasibility, they serve as proof-of-concept demonstrations of relative physiological changes rather than definitive absolute clinical conclusions. Furthermore, systematic tests using heterogeneous phantoms with specific inclusions were not performed to quantitatively evaluate resolution and crosstalk. Therefore, future work will focus on extending the USFDI framework to curved and heterogeneous tissues and integrating independent physiological measurements (e.g., blood flow or tissue hydration) and multi-wavelength systems to enable quantitative chromophore decomposition (e.g., separating hemoglobin and melanin) and further enhance its clinical applicability.

Author Contributions: Conceptualization, X.W. and S.Y.; methodology, X.W.; software, X.W.; validation, X.W. and E.F.; investigation, X.W. and E.F.; resources, E.F.; writing—original draft preparation, X.W.; writing—review and editing, S.Y.; supervision, S.Y.; project administration, S.Y.; funding acquisition, S.Y. All authors have read and agreed to the published version of the manuscript.

Funding: This research was funded by the Heilongjiang Provincial Natural Science Foundation of China (Grant No. PL2026F038) and the Program for Young Talents of Basic Research in Universities of Heilongjiang Province (Grant No. YQJH2024074).

Institutional Review Board Statement: This study was conducted in accordance with the ethical principles of the Declaration of Helsinki. The in vivo experiments involved only the authors as self-experimenters; no external human participants were recruited. No formal ethics committee review or waiver was obtained. All author–participants provided informed consent, and the non-invasive measurements were monitored by another author.

Informed Consent Statement: Informed consent was obtained from all author–participants who served as subjects in the self-experiments.

Data Availability Statement: Data underlying the results presented in this paper are not publicly available at this time but may be obtained from the authors upon reasonable request.

Conflicts of Interest: The authors declare no conflicts of interest. A patent application (Application No. CN202611065192.3) related to this work has been filed by Harbin University of Science and Technology.

References

1. Hirvi, P.; Kuutela, T.; Fang, Q.; Hannukainen, A.; Hyvönen, N.; Nissilä, I. Effects of atlas-based anatomy on modelled light transport in the neonatal head. *Phys. Med. Biol.* **2023**, *68*, 135019. [CrossRef] [PubMed]
2. Lewis, A.V.; Fang, Q. Revisiting equivalent optical properties for cerebrospinal fluid to improve diffusion-based modeling accuracy in the brain. *Neurophotonics* **2025**, *12*, 015009. [CrossRef] [PubMed]
3. Lam, J.H.; Tu, K.J.; Kim, J.; Kim, S. Smartphone-based single snapshot spatial frequency domain imaging. *Biomed. Opt. Express* **2022**, *13*, 6497. [CrossRef] [PubMed]
4. Yang, Y.; Fu, X.; Zhou, Y. Hyperspectral spatial frequency domain imaging technique for soluble solids content and firmness assessment of pears. *Horticulturae* **2024**, *10*, 853. [CrossRef]
5. Yu, S.Q.; Hu, D.; Qiu, D.K.; Jia, T.Z.; Zhou, T.T.; Sun, X.L.; Sun, Z.Z.; Yan, X.J. Profile-based diffuse reflectance corrections for improved optical property measurement of spherical fruit with spatial frequency domain imaging. *Postharvest Biol. Technol.* **2023**, *204*, 112453. [CrossRef]
6. He, X.; Hu, D.; Fu, X.; Rao, X. Spatial frequency domain imaging for determining absorption and scattering properties of bruised pears based on profile corrected diffused reflectance. *Postharvest Biol. Technol.* **2021**, *179*, 111570. [CrossRef]
7. Gao, Y.; Sun, Z.Z.; Luo, X.; Hu, D.; Dai, B.H.; Zheng, Y.J.; Ying, Y.B.; Xie, L.J. Design, characterization, and application of a continuously tunable wavelength spatial frequency domain imaging system for measuring the optical properties of fruits. *Engineering* **2026**, *60*, 49–64. [CrossRef]
8. Liu, M.; Dan, M.; Gao, F. Correction method for spatial frequency domain imaging based on target topography measurement. *Laser Optoelectron. Prog.* **2021**, *58*, 1011027. [CrossRef]

9. Dan, M.; Liu, M.; Bai, W.; Gao, F. Profile-based intensity and frequency corrections for single-snapshot spatial frequency domain imaging. *Opt. Express* **2021**, *29*, 12833. [CrossRef] [PubMed]
10. Wang, Y.K.; Kang, X.; Zhang, Y.; Shi, Z.G.; Ren, H.M.; Wang, Q.F.; Chen, M.W.; Zhang, Y.Z. Wavelength and frequency optimization in spatial frequency domain imaging for two-layer tissue. *Biomed. Opt. Express* **2022**, *13*, 3224–3242. [CrossRef] [PubMed]
11. Chue-Sang, J.; Litorja, M.; Goldfain, A.M.; Germer, T.A. Spatial frequency domain Mueller matrix imaging. *J. Biomed. Opt.* **2022**, *27*, 126003. [CrossRef] [PubMed]
12. Gohma, A.; Adachi, N.; Yonemaru, Y.; Horiba, D.; Higuchi, K.; Nishiwaki, D.; Yokoi, E.; Ue, Y.; Miyawaki, A.; Monai, H. Spatial frequency-based correction of the spherical aberration in living brain imaging. *Microscopy* **2024**, *73*, 37–46. [CrossRef] [PubMed]
13. Lohner, S.A.; Nothelfer, S.; Kienle, A. Generic and model-based calibration method for spatial frequency domain imaging with parameterized frequency and intensity correction. *Sensors* **2023**, *23*, 7888. [CrossRef] [PubMed]
14. Song, A.A.; Chen, M.T.; Bobrow, T.L.; Durr, N.J. Speckle-illumination spatial frequency domain imaging with a stereo laparoscope for profile-corrected optical property mapping. *J. Biomed. Opt.* **2025**, *30*, S13710. [CrossRef] [PubMed]
15. Belcastro, L.; Jonasson, H.; Saager, R.B. Multi-frequency spatial frequency domain imaging: A depth-resolved optical scattering model to isolate scattering contrast in thin layers of skin. *J. Biomed. Opt.* **2024**, *29*, 046003. [CrossRef] [PubMed]
16. Huang, G.; Hu, Y.; Lin, W.; Shen, C.; Yang, J.; Xie, Z.; Ge, Y.; Jin, X.; Qian, X.; Xu, M. Deep-learning-enabled spatial frequency domain imaging of the spatiotemporal dynamics of skin physiology. *J. Biomed. Opt.* **2025**, *30*, 046008. [CrossRef] [PubMed]
17. Sun, Z.; Xie, L.; Hu, D.; Ying, Y. An artificial neural network model for accurate and efficient optical property mapping from spatial-frequency domain images. *Comput. Electron. Agric.* **2021**, *188*, 106340. [CrossRef]
18. Yu, H.; Han, B.; Bai, L.; Zheng, D.; Han, J. Untrained deep learning-based fringe projection profilometry. *APL Photonics* **2022**, *7*, 016107. [CrossRef]
19. Raissi, M.; Perdikaris, P.; Karniadakis, G.E. Physics-informed neural networks: A deep learning framework for solving forward and inverse problems involving nonlinear partial differential equations. *J. Comput. Phys.* **2019**, *378*, 686–707. [CrossRef]
20. Fang, Q.; Yan, S. MCX Cloud—A modern, scalable, high-performance and in-browser Monte Carlo simulation platform with cloud computing. *J. Biomed. Opt.* **2022**, *27*, 083008. [CrossRef]
21. Yan, S.J.; Jacques, S.L.; Ramella-Roman, J.C.; Fang, Q.Q. Graphics processing unit-accelerated Monte Carlo simulation of polarized light in complex three-dimensional media. *J. Biomed. Opt.* **2022**, *27*, 083015. [CrossRef]
22. Ardakani, M.R.; Yu, L.M.; Kaeli, D.; Fang, Q.Q. Framework for denoising Monte Carlo photon transport simulations using deep learning. *J. Biomed. Opt.* **2022**, *27*, 083019. [CrossRef]
23. Dumont, A.P.; Fang, Q.; Patil, C.A. A computationally efficient Monte-Carlo model for biomedical Raman spectroscopy. *J. Biophotonics* **2021**, *14*, e2020000377. [CrossRef] [PubMed]
24. Osman, A.; Crowley, J.; Gordon, G.S.D. Training generative adversarial networks for optical property mapping using synthetic image data. *Biomed. Opt. Express* **2022**, *13*, 5171–5186. [CrossRef] [PubMed]
25. Zhang, Y.; Fang, Q. BlenderPhotonics: An integrated open-source software environment for three-dimensional meshing and photon simulations in complex tissues. *J. Biomed. Opt.* **2022**, *27*, 083014. [CrossRef] [PubMed]
26. Gao, Y.; Sun, Z.; Xie, L.; Ying, Y. Spatial frequency domain imaging for fruit quality assessment: A comprehensive review. *Trends Food Sci. Technol.* **2025**, *162*, 105110. [CrossRef]
27. Cuccia, D.J.; Durkin, A.J.; Bevilacqua, F.; Tromberg, B.J. Quantitation and mapping of tissue optical properties using modulated imaging. *J. Biomed. Opt.* **2009**, *14*, 024012. [CrossRef] [PubMed]
28. Livecchi, T.T.; Jacques, S.L.; Pilvar, A.; Roblyer, D.; Pierce, M.C. Shortwave infrared spatial frequency domain imaging for detection of changes in tissue hydration. *Front. Photonics* **2025**, *6*, 1546952. [CrossRef] [PubMed]

Disclaimer/Publisher's Note: The statements, opinions and data contained in all publications are solely those of the individual author(s) and contributor(s) and not of MDPI and/or the editor(s). MDPI and/or the editor(s) disclaim responsibility for any injury to people or property resulting from any ideas, methods, instructions or products referred to in the content.